

High redshift radio galaxies and divergence from the CMB dipole

Jacques Colin^{1,2}, Roya Mohayaee^{1,2}, Mohamed Rameez², Subir Sarkar^{2,3}

¹ Sorbonne Universités, UPMC Univ Paris 06, CNRS, Institut d’Astrophysique de Paris, 98bis Blvd Arago, Paris 75014, France

² Niels Bohr Institute, University of Copenhagen, Blegdamsvej 17, 2100 Copenhagen Ø, Denmark

³ Rudolf Peierls Centre for Theoretical Physics, University of Oxford, 1 Keble Road, Oxford, OX1 3NP, United Kingdom

18 June 2022

ABSTRACT

Previous studies have found our velocity in the rest frame of radio galaxies at high redshift to be substantially larger than that inferred from the CMB temperature dipole anisotropy. We construct a full sky catalogue NVSUMSS, by merging the NVSS and SUMSS catalogues and removing local sources by various means including cross-correlating with the 2MRS catalogue. We take into account both aberration and Doppler boost to deduce our velocity from the hemispherical number count asymmetry, as well as via a 3-dimensional linear estimator. Both the magnitude and direction depend on cuts made to the catalogue, e.g. on the lowest source flux, however these effects are small. With the hemispheric number count asymmetry method we obtain a velocity of $1729 \pm 187 \text{ km s}^{-1}$ i.e. about 4 times *larger* than that obtained from the CMB dipole, but close in direction, towards RA = $149^\circ \pm 2^\circ$, DEC = $-17^\circ \pm 12^\circ$. With the 3-dimensional estimator, the derived velocity is $1355 \pm 174 \text{ km s}^{-1}$ towards RA = $141^\circ \pm 11^\circ$, DEC = $-9^\circ \pm 10^\circ$. We assess the statistical significance of these results by constructing catalogues of random distributions and show that they are at best significant at the 2.81σ (99.95% confidence) level.

Key words: Cosmology, radio galaxies, Dipole, anisotropy

1 INTRODUCTION

The cosmic microwave background (CMB) exhibits a well-known dipole anisotropy (Bracewell & Conklin 1968; Henry 1971; Smoot et al. 1977) which is three orders of magnitude higher than the primordial temperature fluctuations first detected by COBE (Kogut et al. 1993). An observer moving through an isotropic radiation field would observe such a dipole (Peebles & Wilkinson 1968) and conversely the observed dipole can be used to infer the velocity of the observer. Indeed the velocity of the Solar system (and our Local Group) is inferred from the CMB temperature dipole assuming that the latter is entirely due to our motion.

Although a kinematic origin is the most plausible interpretation of the CMB dipole, one can consider other mechanisms which may be, at least partially, responsible (Paczynski & Piran 1990; Langlois & Piran 1996). An independent measurement of our velocity is therefore desirable. It has been suggested that this can be done by measuring the aberration of the CMB (Challinor & van Leeuwen 2002; Burles & Rappaport 2006), however the effect is too small to be detected with $> 3\sigma$ significance even using the best available data (Planck Collaboration et al. 2014).

If the dipole is due to our motion then it requires the Universe to be anisotropic at least locally. Indeed galaxy

surveys clearly exhibit an anisotropy in the local Universe. Along the direction of the CMB dipole lie the most massive neighbouring superclusters: Virgo, the Great Attractor Hydra-Centaurus, Coma, Hercules and Shapley, and possibly yet-to-be-mapped superclusters beyond these. The gravitational force of these structures could be pulling us in the direction indicated by the CMB dipole. However, maps of the local Universe, e.g. from the infrared 2MASS Redshift Survey (2MRS) or supernova catalogues, have shown that the full dipole *cannot* be attributed to these structures and at least 20% remains unaccounted for (Lauer & Postman 1994; Hudson et al. 2004; Watkins et al. 2009; Lavaux et al. 2010; Feldman et al. 2010; Colin et al. 2011; Magoulas et al. 2012; Feindt et al. 2013; Watkins & Feldman 2015). It is then necessary to go beyond superclusters such as Shapley to search for convergence at larger scales (as is indeed required if the universe is to be described as homogeneous when averaged on such scales). However, there are no full-sky optical galaxy redshift surveys extending well beyond Shapley and previous studies in this context have therefore suffered from lack of full sky coverage (e.g. Plionis et al. (1993); Itoh et al. (2010)). Further complications arise when using other catalogues such as of galaxy clusters to search for the expected dipole signal (e.g. Chluba et al. (2005)).

On the other hand, radio galaxies are extremely luminous, can be observed up to high redshifts, and are unaffected by dust obscuration. However early analyses of the dipole in the distribution of radio galaxies suffered from the severe sparseness of their catalogues (Baleisis et al. 1998). Hence such studies became feasible only after the NRAO VLA Sky Survey (NVSS) catalogue became available. This is a catalogue of nearly 2 million radio galaxies covering the sky above declination of -40° . NVSS has been used extensively to search for convergence to the CMB dipole and most previous studies have found *discrepancy* with the CMB measurement of our local velocity (Singal 2011; Gibelyou & Huterer 2012; Rubart & Schwarz 2013; Tiwari et al. 2015; Tiwari & Jain 2015).

While the velocity of the Solar system barycentre inferred from the CMB temperature dipole anisotropy is 368 km s^{-1} , the value inferred from NVSS ranges from 700 km s^{-1} (Blake & Wall 2002) to over 2000 km s^{-1} (Gibelyou & Huterer 2012). We too find a similarly large velocity and demonstrate that it depends only mildly on the characteristics of the datasets used: *e.g.* the width of the Galactic and supergalactic plane strips removed from the survey and the lower and upper limits of the flux. Significantly the direction of the velocity is quite robust and well-aligned with the direction of the CMB dipole.

It is hard to understand how such a large difference can have a physical explanation. Previous works (Paczynski & Piran 1990; Langlois & Piran 1996; Ghosh 2014) have invoked horizon-scale isocurvature perturbations as an alternative to the kinematic origin for the CMB dipole. Here however, we are observing a dipole far larger than that inferred from CMB itself and at high redshifts. In addition local data — specifically distance and redshift catalogues — indicate that at low redshifts a good part of the CMB dipole is recovered by about 250 Mpc. Although the present data does not allow us to fully explore how the convergence to CMB develops as we go deeper into the Universe and in redshift space, the radio data at redshift $z \sim 1$ clearly indicates that a significantly *larger* dipole exists in the rest frame of the radio galaxies. The origin of this difference from the CMB dipole is a real mystery and deserves closer examination.

A possible explanation is systematics due to the incomplete sky coverage of NVSS which can generate a spurious dipole (Gibelyou & Huterer 2012; Tiwari & Nusser 2016). Various methods have been used to restore the symmetry required for a robust dipole analysis such as cutting the NVSS catalogue above declination of 40° (Singal 2011) or removing the Galactic and counter-Galactic plane (Rubart & Schwarz 2013). Our work elaborates on previous studies in several ways. We construct a *full-sky* catalogue, which we call NVSUMSS, by patching the NVSS with its southern-sky counterpart SUMSS. This results in a catalogue with about 600,000 radio sources with flux above 10 mJy after cutting out a strip of $\pm 10^\circ$ around the Galactic plane in NVSS to match the corresponding cut of SUMSS.

Another possible systematic which has often been discussed is contamination by local sources. It is well known that a large part of the CMB dipole anisotropy is due to the anisotropic local distribution of matter (Lavaux et al. 2010; Colin et al. 2011). Past studies have tried to clean NVSS from such local source contamination either by removing in-

dividual large local structures (Blake & Wall 2002) or by cutting out the super-Galactic plane in which the majority of local superclusters lie (Tiwari et al. 2015). However even after all these cuts the radio dipole extracted by all previous studies remains well above that inferred from the CMB. To fully eliminate the contribution from the local structures, we adopt several strategies. First we cross-correlate NVSUMSS with a catalogue of local radio sources (LRS) (van Velzen et al. 2012) and remove patches (of increasing area) around these sources from NVSUMSS catalogue. Our results are not however significantly altered by doing so. As the LRS catalogue is limited to sources brighter than 200 mJy, we go further by next removing eight dominant local superclusters from Virgo to Ophiuchus. Previous studies have shown that these local structures are responsible for nearly 80% of the CMB dipole. Even so their removal does not alter our results significantly. We then remove the supergalactic plane completely by cutting out a $\pm 10^\circ$ strip around it. This too has little effect. Finally we cross-correlate NVSUMSS with the 2MRS catalogue, and remove zones of increasingly larger areas around the 2MRS sources from the NVSUMSS catalogue. This too has no significant impact.

Because of evolution, the fraction of nearby radio sources is low even at large flux densities, the median redshift of radio sources in complete samples with flux ranging from mJy to Jy being $z \sim 0.8$ (Condon 1989). In practice, however, the fact that the redshift distribution of complete samples of radio sources peaks at $z \sim 1$ for all flux-density levels down to $\sim 10 \text{ mJy}$, implies that local sources are swamped by the much more numerous distant ones (de Zotti et al. 2010). The mean redshift of NVSS sources is estimated to be above 1 (Ho et al. 2008; de Zotti et al. 2010). Thus most of the sources in our NVSUMSS catalogue lie at high redshift and by removing local sources through cross-correlation of NVSUMSS with the 2MRS catalogue we ensure that they constitute an uniform background. Our motion with respect to such an uniform background causes the aberration of light and the sources would thus be displaced in the sky by an angle that depends on our velocity. More sources would be observed in the direction of the motion than in the opposite direction.

Here, by measuring the aberration angle, we infer the velocity of the Solar system (or the Local Group) barycentre in the rest frame of the distant radio galaxies. A catalogue with good sky coverage would exhibit a hemispherical asymmetry which peaks when the plane of hemisphere is perpendicular to the direction of the motion. A simple formula is used to determine the aberration angle and hence our velocity in the rest frame of the radio sources. Aberration analysis is very powerful in the sense that it is *independent* of distance so can be used in conjunction with a full-sky photometric galaxy survey, as long as there are no observational biases that can generate spurious anisotropies. In fact the motion of the observer does not just cause aberration but also results in Doppler boosting which is a shift in the frequency at which the sources are observed — as a result more sources will be observed in the direction of the motion. Unlike aberration, Doppler boosting depends on the flux and it is known that for radio sources the two effects affect the number-count in almost equal proportion.

This paper is organised as follows: in Section 2 we describe our method, and search for dipole anisotropy in the

Table 1. Local superclusters which are responsible for a large part of the CMB dipole (Lavaux et al. 2010; Colin et al. 2011).

Name	{RA°, DEC°}
Virgo	{186.8, 12}
Hydra & Centaurus (Great Attractor)	{192.2, -38}
Norma	{243, -59}
Persus-Pisces	{27.5, 36}
Coma	{195.0, 28.0}
Hercules	{241.3, 17.8}
Shapley	{201.3, -30}
Ophiuchus	{255, -8}

NVSS data alone (Section 3). Then we introduce the SUMSS catalogue (Section 4) and patch NVSS and SUMSS together in Section 5, exploring different ways of doing so. In Section 6 we perform a complete cleaning up of local sources by cross-correlating NVSUMSS with the 2MRS catalogue. We investigate the effects of various cuts made on the inferred dipole velocity and discuss the statistical significance of the result in Section 7. We conclude in Section 8.

2 THE METHOD

The aberration angle, $\Delta\theta$, by which a galaxy is displaced due to the motion of an observer moving with velocity v is (*e.g.* Kopeikin et al. (2011)) for small velocities $v \ll c$:

$$\Delta\theta = (|v|/c) \sin\theta. \quad (1)$$

To evaluate this we simply count the number of galaxies in hemispheres and use the relation of the hemispherical number count asymmetry, δN , to the aberration angle:

$$\Delta\theta = 2(\delta N/N). \quad (2)$$

Here we have assumed a homogeneous distribution with an average number surface density, and not accounted for masks and cuts in the catalogue.

The total number asymmetry is due to both aberration and Doppler boosting. The expected amplitude of the latter is (Ellis & Baldwin 1984): $(v/c)[2+x(1+\alpha)]$, where x and α are flux indices, defined through the integral source counts

$$dN/d\Omega(> S) = kS^{-x}, \quad (3)$$

and the flux density at a fixed observing frequency

$$S_{\text{obs}} = S_{\text{rest}}\delta^{1+\alpha}. \quad (4)$$

It is straightforward to evaluate x for a given catalogue. As shown in Fig. 1 the exponent x is not constant and varies from 0.894 at low flux to 1.681 at high flux for NVSS. The Doppler shift is more important for faint galaxies, hence the value at low flux is relevant. The value of α is usually taken to be 0.75 (Ellis & Baldwin 1984). Hence the aberration and Doppler boosting contribute almost equally to the number count asymmetry — 53% and 47% respectively.

As we are looking specifically for a dipole anisotropy (to compare with the CMB dipole), we do not use spherical harmonic decomposition as used previously. The simplest and most robust estimate of the dipole is in fact obtained by looking for a hemispheric asymmetry in the number count of sources. We do this by the following methods: First by randomly selecting a direction and calculating the number of galaxies in that hemisphere. Second by regularly rotating a hemisphere centred on zero declination and looking for the right ascension that gives the maximum asymmetry. Third by scanning the sky using directions from a HEALPix map (Gorski et al. 2004) with $N_{\text{side}} = 32$ (12,288 pixels) which are not random directions but regularly spaced. As we shall show, all these methods give similar results in agreement with each other. While the hemispheric asymmetry estimator is robust and allows the estimation of the variability of the dipole around its directional maximum, its statistical variability is high. Hence, we also evaluate the dipole using a 3-dimensional linear estimator (Crawford 2009).

3 NRAO VLA SKY SURVEY (NVSS)

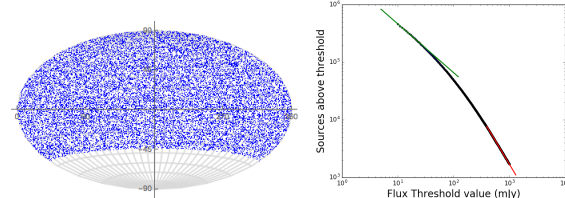


Figure 1. NVSS: The left panel is the plot of the RA and DEC in aitoff projection of the full NVSS catalogue without any cut in flux or sky. The right panel shows how the NVSS flux changes with the lower cut in frequency which we use to determine the power x in eq. (3), finding it to be 0.894 and 1.681 at lower and higher edges.

The NVSS is a catalogue of radio sources at 1.4 GHz which cover the sky north of declination -40° (the lowest source is actually at $\text{DEC} = -40.4^\circ$) corresponding to 82% of the celestial sphere (Condon 1989). It contains 1,773,488 sources stronger than a flux density of about 2.5 mJy. However, we restrict our analysis to sources brighter than 10 mJy as the completeness of the survey at weaker flux-density levels is questionable (Overzier et al. 2003). We also restrict the source brightness to be below 1000 mJy as a relatively small number of strong sources at high flux-density levels can introduce large statistical fluctuations.

We further cut the catalogue above $\text{DEC} = 40^\circ$ in order to restore the symmetry necessary for studying the dipole (Singal 2011). The catalogue is shown in the left panel of Fig. 1. The right panel of the same figure shows how the flux changes with the lower cut in frequency which we use to determine the power x in eq. (3), finding it to be 0.894 and 1.681 at lower and higher edges for NVSS. We cut the Galactic plane by $\pm 5^\circ$, and then by $\pm 10^\circ$, and study the resulting catalogues adopting lower flux cuts of 10, 15, 20 and 25 mJy.

The results of our hemispheric asymmetry analysis are

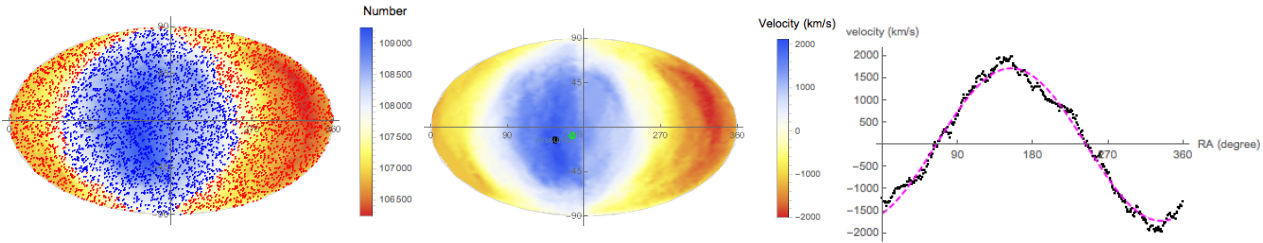


Figure 2. NVSS: The left panel shows the directions of 5000 randomly selected hemispheres which are used for number counts. The blue dots represent hemispheres with more-than-average number of galaxies, while red dots indicate those with less-than-average number of galaxies. The middle panel is a density plot of the magnitude of the velocity, upon which the directions of the CMB dipole (green circle) and the inferred direction for the radio sources (black circle) are marked. The right panel is the plot of the derived velocities (black dots) against the RA, which is fitted well by a cosine curve (magenta).

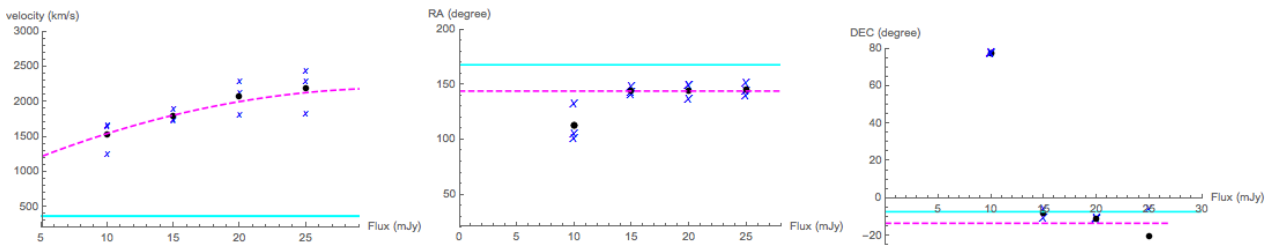


Figure 3. NVSS: Our results for the dipole velocity magnitude and direction with various Galactic and supergalactic cuts, and also with the Local radio Sources (LRS) and the 2MRS sources removed and different patching schemes (black crosses). The black circles are the mean values at each flux and the dashed line is the fit to the mean, given by the quadratic $|v| = 823 + 86S - 1.34S^2$ where S is the lower cutoff in flux in mJy. Magenta dashed lines are the least-squares fits which give a mean velocity of $1918 \pm 298 \text{ km s}^{-1}$ in the direction RA=147°, DEC=−18.5°. The solid cyan line is the corresponding value inferred from CMB temperature dipole.

shown in Tables 2 and 3 and in Fig. 2. The results presented in Fig. 2 are obtained by cutting the NVSS area above DEC= 40° to match the missing southern part below DEC= −40°, and the Galactic plane is also cut at ±10°. The dipole direction in all cases is close to that of the CMB dipole but its magnitude is on average about 4 times larger than that for the CMB (see Fig. 3).

4 SYDNEY UNIVERSITY MOLONGLO SKY SURVEY (SUMSS)

The Sydney University Molonglo Sky Survey (SUMSS) is a radio imaging survey of the sky south of declination, $\delta \leq -30^\circ$ carried out with the Molonglo Observatory Synthesis Telescope (MOST) operating at 843 MHz (Mauch et al. 2003). SUMSS contains 211,050 radio sources and is similar in sensitivity and resolution to the NVSS. Analysis of the catalogue shows that it is highly uniform and complete to 8 mJy at $\delta \leq -50^\circ$, and to 18 mJy at $\delta > -50^\circ$. An Aitoff plot of the catalogue is shown in Fig. 4.

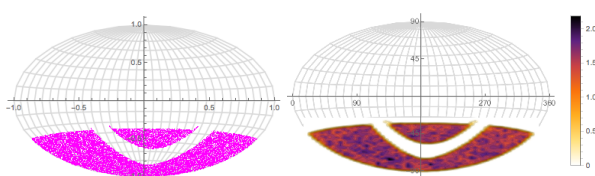


Figure 4. SUMSS: The SUMSS catalogue (left) and its density plot (right).

For a robust dipole analysis a *full-sky* catalogue is necessary, so we combine the NVSS and SUMSS surveys. There are different ways of patching the two catalogues together which can potentially yield different results. This is discussed in the next section.

5 FULL SKY CATALOGUE: NVSS PATCHED WITH SUMSS (NVSUMSS)

We fill in the missing sky in NVSS to obtain a full-sky catalogue by combining it with its southern counterpart SUMSS. To address overlapping regions, we generate the composite catalogue in two ways. In the first, SUMSS is cut at DEC= −40° and joined to NVSS, while in the second NVSS is cut at DEC= −30° and joined to SUMSS, as shown in Fig. 5. The right panel of Fig. 5 shows how the flux changes with the lower cut in frequency which we use to determine the power x in eq. (3). For NVSUMSS we find it to be 0.9 (cf. 0.894 for NVSS) and 1.7 (cf. 1.681 for NVSS) at the lower and higher edges.

Furthermore, NVSS and SUMSS have different source densities with SUMSS being denser. In order to achieve the same density we again adopt two approaches. In the first, we randomly select galaxies from the SUMSS catalogue below DEC= −40° (or below −30°) to match the same number as NVSS above Dec= 40° (or 30°). In the second approach we evaluate the source density of NVSS in the full catalogue, and also that of SUMSS, and then pick randomly from SUMSS such that its density matches that of NVSS. Although in the former patching scheme we run the risk of smoothing out any dipole lying in the cap regions, as we

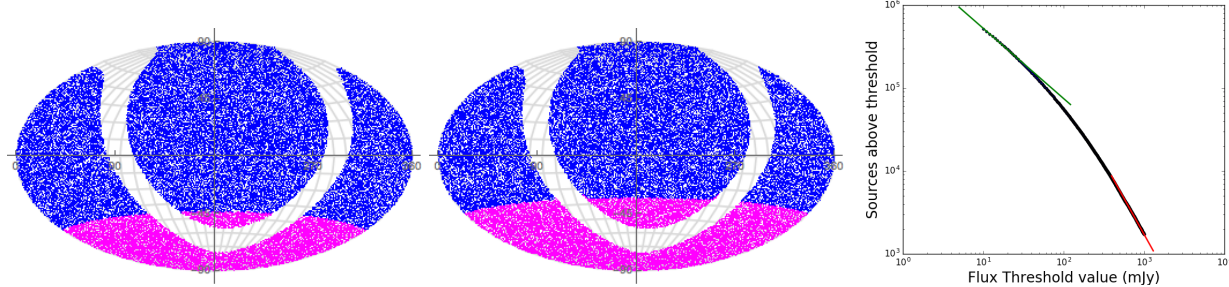


Figure 5. NVSUMSS: The left panel shows SUMSS cut at $\text{DEC} = -40^\circ$ and joined with NVSS, while the middle panel shows NVSS cut at $\text{DEC} = -30^\circ$ and joined with SUMSS. The right panel shows the number of sources in NVSUMSS above a flux threshold as a function of the latter. Also shown is the fit of eq. (3) at low and high flux which yields x of 0.9 and 1.7 respectively

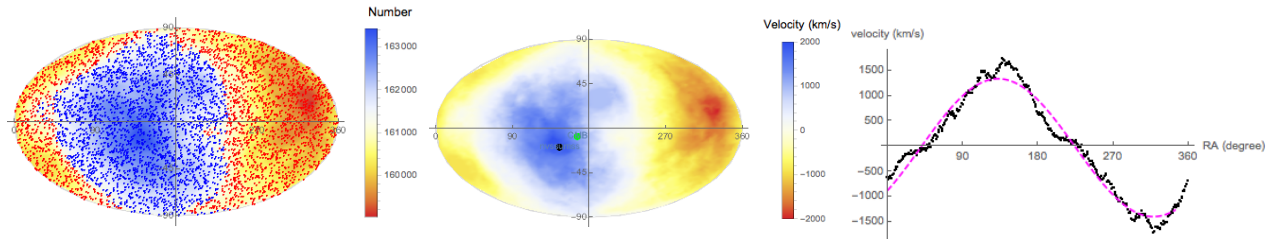


Figure 6. NVSUMSS catalogue (20–1000 mJy): NVSS catalogue with SUMSS (cut at $\text{DEC} = -40^\circ$) and the Galactic plane cut at latitude of $\pm 10^\circ$ off NVSS to match the cut of SUMSS. The left panel shows number counts in 5000 randomly oriented hemispheres with an average of 288,218 galaxies per hemisphere and maximum difference of 5672 between the most and least populated hemispheres. The blue dots represent hemispheres which contain more-than-average number of galaxies, while red dots indicate those with less-than-average number of galaxies. The middle panel is a density plot of the magnitude of the velocity, upon which the directions of the CMB dipole (green circle) and the inferred direction for the radio sources (black circle) are marked. The right panel is the plot of inferred velocities (black dots) against the RA, which is fitted well by a cosine curve (magenta).

shall show these different ways of producing the composite catalogue in fact yield rather similar results. The radio dipole still implies a large velocity in a direction close to that of the CMB dipole, as shown in Tables 4 and 5 and in Figs. 6 and 7.

To ensure that the Galactic plane is not producing spurious effects on the inferred radio dipole, we also fill the Galactic plane with a random distribution of sources having the same surface density as the NVSUMSS catalogue. Our results are given in Table 6 and Figure 7 shows that the results do not change significantly.

6 DEALING WITH LOCAL ANISOTROPY

Any clustering of nearby sources can invalidate our approach, as both aberration and Doppler boosting analysis rely on the source distribution being isotropic so the only anisotropy is due to the observer's motion. Since the NVSS and SUMSS sources are mainly at redshift $z \sim 1$ (de Zotti et al. 2010; Ho et al. 2008) local anisotropies must be minimal, nevertheless we guard against them carefully as follows.

First we cross-correlate our composite NVSUMSS catalogue with the catalogue of nearby radio sources (van Velzen et al. 2012). However, the latter only contains bright radio-galaxies. In order to make sure that our composite catalogue is cleaned of *all* local sources, we go even further. We identify all local superclusters up to the Shapley concentration and remove them from NVSUMSS. Next we remove the su-

pergalactic plane in which most dominant local structures lie. The final removal of all local sources is achieved by cross-correlating NVSUMSS with the 2MRS catalogue. We thus ensure as best as we can that *no* nearby sources are left in our composite catalogue.

6.1 Cross correlation of NVSUMSS with LRS

The radio sources from the NVSS and SUMSS surveys have been matched to 2MRS galaxies using an image-level algorithm that properly treats the extended structure of radio sources (van Velzen et al. 2012). These bright sources constitute the all-sky Local Radio Sources (LRS) catalogue containing 575 radio-emitting galaxies with flux greater than 213 mJy at 1.4 GHz. However this means that nearby sources with flux less than 213 mJy are *not* identified and we shall address this in the following subsections. Here, we cross-correlate the LRS catalogue with our composite NVSUMSS catalogue and remove zones of increasingly larger area, starting at $1/10^\circ$ then $1/4^\circ$ then $1/2^\circ$, around the LRS sources. The results of the cross-correlation are presented in Table 7. The dipole of the LRS, using hemispherical number count, is shown in Fig. 8. The figure is to emphasise that the contribution of LRS sources to the large-scale dipole observed in NVSS and NVSUMSS is insignificant.

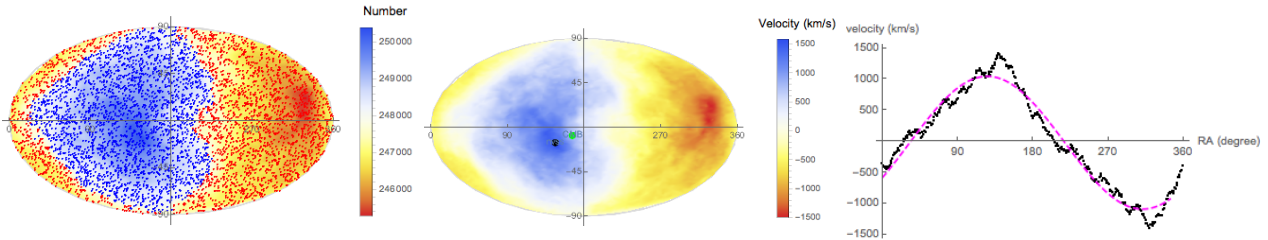


Figure 7. NVSUMSS with the Galactic plane filled with a random distribution having the same number density as the rest of the catalogue. The flux range is 15–1000 mJy and the details of the catalogues used in this figures are given in Table 6. The left panel shows the directions of hemispheres with blue corresponding to those having average count greater than mean and red to those with average count less than the mean. The middle panel is the magnitude of the velocity inferred from the number-count hemispherical asymmetry. The right panel is obtained by regularly rotating hemispheres in the RA direction at a 1° interval.

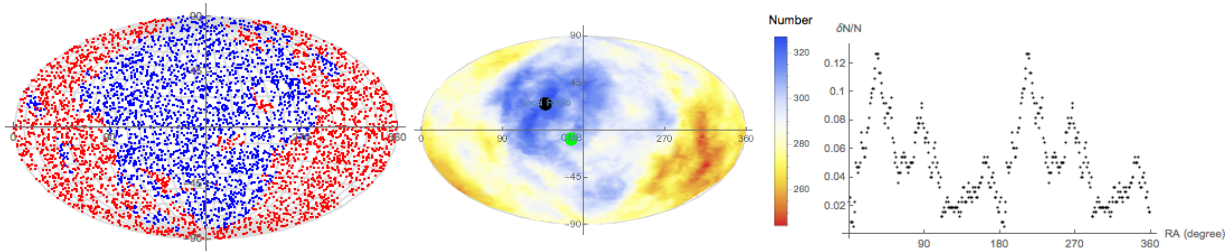


Figure 8. Local Radio Sources (LRS): The left panel shows the directions of 5000 randomly placed hemispheres in the LRS catalogue of 575 radio galaxies in the local universe, with blue corresponding to those having average count greater than the mean (of 288) and red to those with average count less than the mean. The middle panel shows that a meaningful dipole cannot be seen in such a sparse and inhomogeneous sample. This is illustrated further in the right panel which plots the fractional number count difference between the forward and backward hemispheres versus the RA of the chosen direction.

6.2 Elimination of large superclusters up to Shapley and Ophiuchus

The origin of the CMB dipole is supposedly due to the gravitational attraction of nearby inhomogeneities. A large part of it can indeed be attributed to local superclusters (Lavaux et al. 2010; Colin et al. 2011). These superclusters are well observed and their position are indicated in Table 1. (We note that in a previous study (Blake & Wall 2002) 22 local sources were removed however it is not clear what these sources were.) The results presented in Table 8 show that the dipole velocity is not affected by these eliminations.

6.3 Removing the supergalactic plane

The most important superclusters in our local Universe define the supergalactic plane which may contain a significant number of radio sources (Shaver & Pierre 1989). Hence one way of removing local sources is to remove this plane. Fig. 9 shows the NVSUMSS map with both the Galactic and supergalactic planes cut out as $\pm 10^\circ$ strips. However this makes little difference to either the magnitude or the direction of the radio dipole as seen from the results in Tables 9 and 10.

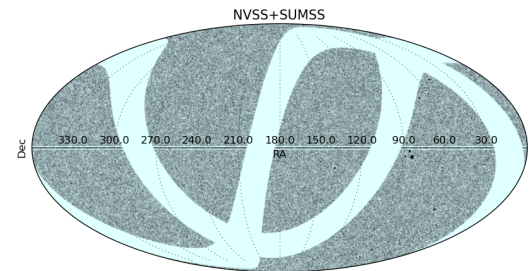


Figure 9. NVSUMSS with Galactic and supergalactic planes removed by a strip of $\pm 10^\circ$ each.

6.4 Cross correlation of NVSUMSS with 2MRS

There could still be local sources not lying on the supergalactic plane, or not included in our list of prominent superclusters, or with flux less than 213 mJy. In order to be certain that *all* local sources have indeed been removed, we cross-correlate NVSUMSS with the 2MRS catalogue (Huchra et al. 2012) and remove all common objects. This is done by identifying all NVSUMSS sources that are within a chosen angular distance of 2MRS sources — we try various values: 1, 10 and 36 arc seconds. The full set of all results are shown in Figures 10 and 11 and all details are also given in Tables 9 and 10. These demonstrate that dipole velocity of these radio galaxies remains well above that given by the CMB dipole anisotropy, although the direction remains close.

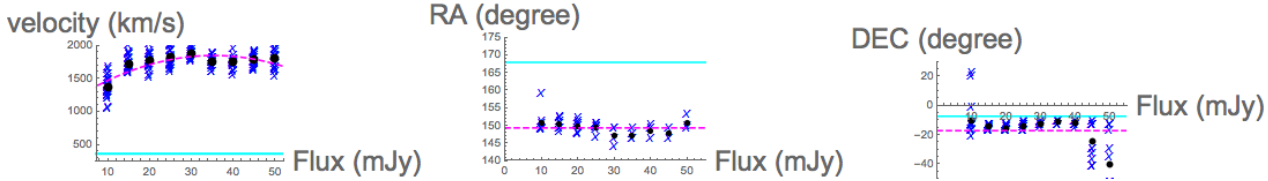


Figure 10. All results from NVSUMSS using the hemispherical number count estimator, with the Galactic and supergalactic plane cut out, and with Local Radio Sources (LRS) as well as 2MRS sources removed, and using different patching schemes (blue crosses). The black filled circles are the means for each flux and the dashed line is the least-squares fit to the data which yields the velocity $|v| = 1121 + 41S - 0.6S^2$ where S is the lower cutoff in the flux in mJy. The cyan line is the value inferred from CMB temperature dipole.

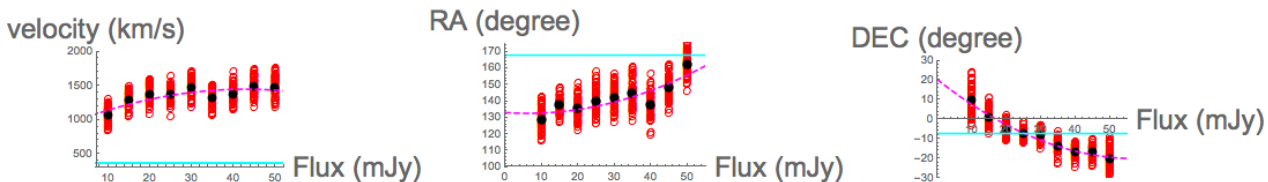


Figure 11. All results from NVSUMSS using the linear 3d estimator, with the Galactic and supergalactic plane cut out, and with LRS as well as 2MRS sources removed, and using different patching schemes (red circles). The black filled-circles are the means for each lower flux-cut and the dashed line is the least-squares fit to the data which yields the velocity $|v| = 926.7 + 24.4S - 0.28S^2$ where S is the lower cutoff in the flux in mJy. The cyan line is the value inferred from CMB temperature dipole.

7 STATISTICAL SIGNIFICANCE

To determine the statistical significance of our results, we compare them with Monte Carlo simulations using randomly generated isotropic catalogues, on top of which aberration and Doppler boosting dipoles can be added according to the null hypothesis that we are traveling w.r.t. the CMB with a velocity of 368 km s^{-1} towards $l=263.85^\circ$, $b=48.25^\circ$. A sample of size N is expected to contain random hemispherical asymmetries of size $\sim 1/\sqrt{N}$ on average, the direction of the dipole being completely random. An aberration effect corresponding to what is expected from our velocity of 368 km s^{-1} with respect to the CMB is subsequently applied to these catalogues by shifting the angles in the direction of the CMB dipole by the expected amount. A dipole due to Doppler boosting can also be incorporated by adding (subtracting) the appropriate number of sources within angular rings oriented in (opposite to) the direction of the CMB dipole. The hemispheric asymmetry and 3-dimensional linear estimators can be subsequently applied to the resultant random catalogues to extract the velocity.

In 2000 mock catalogues with about 600,000 sources generated as above, the hemispheric count estimator observed velocities larger than the inferred 1600 km s^{-1} for 741 of these. The inferred dipole direction was within 15° of the (simulated) CMB dipole direction for 690 of these. For the same 2000 catalogues, the 3-dimensional linear estimator found velocities higher than the inferred 1300 km s^{-1} for only 5 of the catalogues, all of which had dipole directions within 10° of the (simulated) CMB dipole direction. Consequently, the statistical significance of the latter observation is at the level of $p \simeq 0.0025$, i.e 2.81σ .

8 CONCLUSION

The velocity of the barycentre of our Solar system (or of the Local Group) in the rest frame of CMB is inferred from

its temperature dipole anisotropy. An independent measurement of this velocity is needed to fully establish the kinematical origin of the dipole. Although a similar anisotropy is observed in the distribution of nearby large-scale structure out to the Shapley supercluster at redshift $z \simeq 0.06$ (~ 260 Mpc), they do *not* show full convergence to the CMB dipole. To definitively address this question one thus needs to go further, however there is no data available from optical or infrared galaxy surveys.

Radio surveys which sample the Universe at high redshifts provide valuable clues to this problem. As these scales are certainly large enough for the Universe to be considered homogeneous and isotropic (aside from negligible statistical fluctuations), the only source of deviation from isotropy would be due to the motion of the observer. Our motion would lead to a measurable overdensity of sources in the direction of motion through aberration and Doppler boosting effects. By measuring these effects we can deduce our velocity in the rest frame of the radio galaxies, its expected value being just our velocity in the CMB rest frame. NVSS is a radio catalogue with less-than-complete sky coverage which has been used extensively to extract this velocity but previous studies have generally found it value to be far larger than our velocity in the CMB rest frame. We confirm this result using an all-sky catalogue.

A possible reason for this could be bias due to local structures. Of course one does not expect such anisotropies to produce a dipole *larger* than the CMB dipole. However we know that our local Universe at least up to 260 Mpc ($z \simeq 0.06$) is anisotropic and if our radio catalogue is contaminated by local sources, that may invalidate the method based on the aberration and Doppler boosting effects which rely on large-scale intrinsic isotropy. We adopt various measures to remove such local sources but find that this has little effect on the inferred radio dipole.

There is a big gap in redshift between local galaxies and the radio galaxies. Forthcoming galaxy surveys will progres-

sively fill in this gap and hopefully allow us to trace the divergence from the CMB dipole. Also future radio surveys with the Square Kilometre Array (SKA) will provide excellent opportunities for improving the statistical significance of the unexpectedly large radio dipole.

RM and JC acknowledges support from the Nordea Foundation and hospitality at the Niels Bohr International Academy. This work was supported by a DNRF Niels Bohr Professorship awarded to SS. We thank Pavel Naselsky, Andy Jackson and van Velzen for very helpful discussions.

REFERENCES

- Planck Collaboration, Aghanim N., Armitage-Caplan C. et al., 2014, *A&A*, 571, A27
- Baleisis A., Lahav O., Loan A. J., Wall J. V., 1998, *MNRAS*, 297, 545
- Blake C., Wall J., 2002, *Nature*, 416, 150
- Bracewell R. N., Conklin E. K., 1968, *Nature*, 219, 1343
- Burles S., Rappaport S., 2006, *ApJ*, 641, L1
- Challinor A., van Leeuwen F., 2002, *Phys. Rev. D* 65, 103001
- Chluba, J., Hütsi G., Sunyaev R. A., 2005, *A&A*, 434, 811
- Colin J., Mohayaee R., Sarkar S., Shafieloo A., 2011, *MNRAS*, 414, 264
- Condon J. J., 1989, *ApJ*, 338, 13
- Crawford F., 2009, *ApJ*, 692, 887
- de Zotti G., Massardi M., Negrello M., Wall J., 2010, *A&A Rev.*, 18, 1
- Ellis G. F. R., Baldwin J. E., 1984, *MNRAS*, 206, 377
- Feindt U., Kerschhaggl M., Kowalski M. et al., 2013, *A&A*, 560, A90
- Feldman H. A., Watkins R., Hudson M. J., 2010, *MNRAS* 407, 2328
- Ghosh S., 2014, *Phys. Rev. D*, 89, 063518
- Gibelyou C., Huterer D., 2012, *MNRAS*, 427, 1994
- Gorski K. M., Hivon E., Banday A. J. et al., 2005, *ApJ*, 622, 759
- Henry, P. S., 1971, *Nature*, 231, 516
- Ho S., Hirata C., Padmanabhan N., Seljak U., Bahcall N., 2008, *Phys. Rev. D*, 78, 043519
- Huchra J. P., Macri L. M., Masters K. L. et al., 2012, *ApJS*, 199, 26
- Hudson M. J., Smith, R. J., Lucey J. R., Branchini E., 2004, *MNRAS* 352, 61
- Itoh Y., Yahata K., Takada M., 2010, *Phys. Rev. D*, 82, 043530
- Kogut A., Lineweaver C., Smoot G. F. et al., 1993, *ApJ*, 419, 1
- Kopeikin S., Efroimsky M., Kaplan G. 2011, Relativistic Celestial Mechanics of the Solar System, by S. Kopeikin, M. Efroimsky and G. Kaplan, Wiley, 2011..
- Langlois D., Piran T., 1996, *Phys. Rev. D*, 53, 2908
- Lauer T. R., Postman M., 1994, *ApJ* 425, 418
- Lavaux G., Tully R. B., Mohayaee R., Colombi S., 2010, *ApJ*, 709, 483
- Magoulas C., Springob C., Colless M., Jones D. H., Campbell L., Lucey J., Mould J., 2012, AAO Observer Number 122, pp.10-12, ArXiv e-prints 1210.0625
- Mauch T., Murphy T., Buttery H. J., et al., 2003, *MNRAS*, 342, 1117
- Overzier R. A., Röttgering H. J. A., Rengelink R. B., Wilman R. J., 2003, *A&A*, 405, 53
- Paczynski B., Piran T., 1990, *ApJ*, 364, 341
- Peebles P. J. E., Wilkinson David T., 1968, *Phys. Rev. D*, 174, 2168
- Plionis M., Coles P., Catelan P., 1993, *MNRAS*, 262, 465
- Rubart M., Schwarz D. J., 2013, *A&A*, 555, A117
- Shaver P. A., Pierre M., 1989, *A&A*, 220, 35
- Singal A. K., 2011, *ApJ*, 742, L23
- Smoot G. F., Gorenstein M. V., Muller R. A., 1977, *Phys. Rev. Lett.*, 39, 898
- Tiwari P., Jain P., 2015, *MNRAS*, 447, 2658
- Tiwari P., Kothari R., Naskar A., Nadkarni-Ghosh S., Jain P., 2015, *Astroparticle Physics*, 61, 1
- Tiwari P., Nusser A., 2016, *Journal of Cosmology and Astroparticle Physics*, 3, 062
- van Velzen S., Falcke H., Schellart P., Nierstenhöfer N., Kampert K.-H., 2012, *A&A*, 544, A18
- Watkins R., Feldman H. A., Hudson M. J., 2009, *MNRAS*, 392, 743
- Watkins R., Feldman H. A., 2015, *MNRAS*, 447, 132

Table 2. Hemispheric Asymmetry, NVSS (with Northern cap removed at DEC=40° for symmetry with the missing southern part. Uses 5000 random hemispheres): Galactic Latitude Cut (\pm), Flux threshold (mJy), Total Number of sources left after cuts, Average numbers in each hemispheres \bar{N} , Maximum difference in number count of hemispheres ΔN , dipole RA (deg), dipole DEC (deg), Velocity (km s $^{-1}$)

b cut	Flux cut	N	\bar{N}	ΔN	RA°	DEC°	v (km/s)
5	10	416389	208180	4580	100.6	77.1	1657.5
5	15	299409	149704	3762	142.9	-6.1	1899.2
5	20	233277	116631	3565	148.2	-10.8	2294.9
5	25	189995	95012	3081	150.6	-35.1	2438.8
10	10	384844	192391	4096	104.6	77.3	1644.8
10	15	276524	138281	3220	148.1	-10.9	1732.6
10	20	215418	107725	3018	148.9	-11.5	2119.2
10	25	175383	87713	2690	143.9	-5.9	2296.4

Table 3. Hemispheric Asymmetry, NVSS (with Northern cap removed at DEC=40° for symmetry with missing southern part. Using HEALPix grid of Nside=32): Supergalactic latitude cut (\pm), Galactic Latitude Cut (\pm), Flux threshold (mJy), Total Number of sources left after cuts, dipole DEC (deg), dipole RA (deg), dipole b (deg), Galactic l (deg), Velocity (km s $^{-1}$)

SGB cut	b cut	Flux cut	N	DEC°	RA°	D	b°	l°	v (km/s)
0	5	10	413254	76.8	105.0	0.012	26.8	137.7	1502
0	5	15	297806	-17.0	150.5	0.013	29.7	255.0	1668
0	5	20	232256	-32.8	153.3	0.016	19.2	268.4	2054
0	5	25	189357	-32.8	153.3	0.017	19.2	268.4	2183
0	10	10	381951	76.8	105.0	0.011	26.8	137.7	1447
0	10	15	275168	-15.7	149.1	0.012	29.7	252.9	1530
0	10	20	214643	-17.0	147.7	0.014	27.8	252.8	1859
0	10	25	174881	-6.0	143.4	0.015	31.9	240.1	1992
5	5	10	384647	76.8	105.0	0.012	26.8	137.7	1619
5	5	15	277131	-17.0	150.5	0.013	29.7	255.0	1682
5	5	20	216046	-32.8	153.3	0.015	19.2	268.4	2002
5	5	25	176136	-32.8	153.3	0.016	19.2	268.4	2105
5	10	10	353344	76.8	105.0	0.012	26.8	137.7	1569
5	10	15	254493	-15.7	149.1	0.012	29.7	252.9	1535
5	10	20	198433	-17.0	147.7	0.014	27.8	252.8	1785
5	10	25	161660	-6.0	143.4	0.015	31.9	240.1	1891
10	5	10	356540	58.9	139.3	0.012	41.6	156.6	1532
10	5	15	256877	-17.0	150.5	0.013	29.7	255.0	1703
10	5	20	200321	-32.8	153.3	0.015	19.2	268.4	2000
10	5	25	163267	-32.8	153.3	0.016	19.2	268.4	2081
10	10	10	325237	76.8	105.0	0.011	26.8	137.7	1432
10	10	15	234239	-15.7	149.1	0.012	29.7	252.9	1546
10	10	20	182708	-17.0	147.7	0.014	27.8	252.8	1765
10	10	25	148791	-6.0	143.4	0.014	31.9	240.1	1846

Table 4. Hemispheric Asymmetry, NVSUMSS (uses 5000 random hemispheres): Galactic Latitude Cut (\pm), NVSS-SUMSS patch declination, Flux threshold (mJy), Total number of sources left after cuts, Average numbers in each hemispheres \bar{N} , Maximum difference in number count of hemispheres ΔN , dipole DEC (deg), dipole RA (deg), Velocity (km s $^{-1}$)

b cut	patch cut	Flux cut	N	\bar{N}	ΔN	DEC $^{\circ}$	RA $^{\circ}$	v (km/s)
10	-40.	10	576461	288212	5880	151.3	-16.5	1570.9
10	-40.	15	413838	206932	5165	148.2	-13.1	1861.6
10	-40.	20	322452	161229	4422	148.0	-16.8	2056.1
10	-40.	25	262617	131297	3538	149.8	-12.9	1990.5
10	-30.	10	576617	288311	6468	148.8	-1.3	1673.0
10	-30.	15	413564	206768	5456	152.6	-17.4	1999.9
10	-30.	20	322074	161020	4304	151.3	-15.0	2017.6
10	-30.	25	262332	131149	3510	149.5	-13.3	2005.9

Table 5. Hemispheric Asymmetry, NVSUMSS (using HEALPix grid of Nside=32): Supergalactic latitude cut (\pm), Galactic Latitude Cut (\pm), NVSS-SUMSS patch declination, Flux threshold (mJy), Total Number of sources left after cuts, dipole DEC (deg), dipole RA (deg), dipole value, Galactic b (deg), Galactic l (deg), Velocity (km s $^{-1}$)

SGB cut	b cut	patch cut	Flux cut	N	DEC $^{\circ}$	RA $^{\circ}$	D	b	l	v (km/s)
0	10	-40	10	571017	-13.2	149.1	0.0084	31.4	250.8	1094
0	10	-40	15	410966	-13.2	149.1	0.0111	31.4	250.8	1436
0	10	-40	20	320577	-17.0	150.5	0.0117	29.7	255.0	1520
0	10	-40	25	261293	-17.0	150.5	0.0128	29.7	255.0	1656
0	10	-30	10	571982	-13.2	149.1	0.0076	31.4	250.8	987
0	10	-30	15	411258	-13.2	149.1	0.0109	31.4	250.8	1409
0	10	-30	20	320651	-17.0	150.5	0.0118	29.7	255.0	1530
0	10	-30	25	261363	-17.0	150.5	0.0113	29.7	255.0	1461
5	10	-40	10	517269	-13.2	149.1	0.0090	31.4	250.8	1169
5	10	-40	15	372124	-17.0	150.5	0.0113	29.7	255.0	1463
5	10	-40	20	290194	-15.7	151.9	0.0116	31.5	255.1	1507
5	10	-40	25	236448	-10.8	146.3	0.0124	31.0	246.5	1609
5	10	-30	10	518021	-13.2	149.1	0.0088	31.4	250.8	1143
5	10	-30	15	372370	-17.0	150.5	0.0108	29.7	255.0	1397
5	10	-30	20	290249	-17.0	147.7	0.0111	27.8	252.8	1438
5	10	-30	25	236574	-13.2	149.1	0.0115	31.4	250.8	1486
10	10	-40	10	464161	-13.2	149.1	0.0100	31.4	250.8	1295
10	10	-40	15	334073	-13.2	149.1	0.0129	31.4	250.8	1673
10	10	-40	20	260580	-14.5	150.5	0.0118	31.5	253.0	1529
10	10	-40	25	212239	-10.8	146.3	0.0120	31.0	246.5	1551
10	10	-30	10	464926	-13.2	149.1	0.0098	31.4	250.8	1265
10	10	-30	15	334335	-13.2	149.1	0.0127	31.4	250.8	1646
10	10	-30	20	260539	-13.2	149.1	0.0118	31.4	250.8	1530
10	10	-30	25	212219	-13.2	149.1	0.0116	31.4	250.8	1503

Table 6. Hemispheric Asymmetry, NVSUMSS (with Galactic plane filled with a random distribution; uses 5000 random hemispheres): Galactic Latitude Cut (\pm), NVSS-SUMSS patch declination, Flux threshold (mJy), Total Number of sources left after cuts, Average numbers in each hemispheres \bar{N} , Maximum difference in number count of hemispheres ΔN , dipole RA (deg), dipole DEC (deg), Velocity (km s $^{-1}$)

b cut	patch cut	Flux cut	N	\bar{N}	ΔN	RA°	DEC°	v (km/s)
10	-40	10	689995	345007	5743	149.0	-14.3	1306.3
10	-40	15	495573	247804	5164	149.2	-13.8	1590.6
10	-40	20	386549	193283	4428	150.0	-17.3	1722.6
10	-40	25	314213	157107	4200	148.8	-13.3	2003.6
10	-30	10	690314	345146	6954	159.0	-20.9	1512.8
10	-30	15	495366	247685	5432	152.3	-16.2	1647.3
10	-30	20	385862	192957	4371	152.3	-16.2	1711.2
10	-30	25	313849	156947	4193	149.6	-14.5	2006.9

Table 7. Hemispheric Asymmetry, NVSUMSS (uses 5000 random hemispheres): area in degree 2 around sources in LRS which is removed from NVSUMSS, Galactic Latitude Cut(\pm), NVSS-SUMSS patch declination, Flux threshold (mJy), Total Number of sources left after cuts, Average numbers in each hemispheres \bar{N} , Maximum difference in number count of hemispheres ΔN , dipole RA (deg), dipole DEC (deg), Velocity (km s $^{-1}$). In total between 2000 and 4000 sources are removed.

Area cut	b cut	patch cut	flux cut	N	\bar{N}	ΔN	RA°	DEC°	v (km/s)
$1/10^{\circ 2}$	10	-40.	15	411828	205918	5275	150.2	-13.8	1922.4
$1/4^{\circ 2}$	10	-40.	15	410745	205369	5072	150.6	-17.4	1842.4
$1/2^{\circ 2}$	10	-40.	15	409027	204511	4745	152.5	-17.2	1768.7

Table 8. Hemispheric Asymmetry, NVSUMSS (uses 5000 random hemispheres): area in degree 2 around the 8 local superclusters (see Table 1), Galactic Latitude Cut (\pm), NVSS-SUMSS patch declination, Flux threshold (mJy), Total Number of sources left after cuts, Average numbers in each hemispheres \bar{N} , Maximum difference in number count of hemispheres ΔN , dipole RA (deg), dipole DEC (deg), Velocity (km s $^{-1}$). In total about 5000 to 6000 sources are removed.

Area cut	b cut	patch cut	flux cut	N	\bar{N}	ΔN	RA°	DEC°	v (km/s)
$1/10^{\circ 2}$	10	-40	15	409025	204477	4709	151.4	-16.5	1788.5
$1/4^{\circ 2}$	10	-40	15	409011	204488	4885	151.4	-16.4	1805.5
$1/2^{\circ 2}$	10	-40	15	408989	204492	4683	146.8	-12.8	1703.6

Table 9. Hemispheric Asymmetry, NVSUMSS cross-correlated with 2MRS to remove local sources (using HEALPix grid of Nside=32) (1) Angular tolerance within which 2MRS sources are looked for, (2) Number of sources removed because of 2MRS overlap, (3) Supergalactic latitude cut(\pm), (4) Galactic Latitude Cut(), (5) NVSS-SUMSS patch declination, (6) Flux threshold (mJy), (7) Total Number of sources left after cuts, (8) dipole DEC(deg), (9) dipole RA(deg), (10) dipole value, (11) Galactic b (deg), (12) Galactic l (deg), (13) Velocity (km s^{-1})

(1)	(2)	(3)	(4)	(5)	(6)	(7)	(8)	(9)	(10)	(11)	(12)	(13)
\dots / \dots												
10"	1387	0	10	-40	35	187710	-10.8	146.3	0.011	31.0	246.5	1751
10"	1223	0	10	-40	40	163844	-13.2	149.1	0.011	31.4	250.8	1796
10"	1080	0	10	-40	45	144974	-13.2	149.1	0.011	31.4	250.8	1698
10"	973	0	10	-40	50	129691	-30.0	153.3	0.011	21.5	266.6	1725
10"	4746	0	10	-30	10	567241	-13.2	149.1	0.007	31.4	250.8	1048
10"	3269	0	10	-30	15	407972	-13.2	149.1	0.011	31.4	250.8	1676
10"	2446	0	10	-30	20	318182	-17.0	147.7	0.011	27.8	252.8	1683
10"	1955	0	10	-30	25	259403	-17.0	150.5	0.010	29.7	255.0	1597
10"	1623	0	10	-30	30	218268	-13.2	149.1	0.011	31.4	250.8	1798
10"	1373	0	10	-30	35	187615	-10.8	146.3	0.011	31.0	246.5	1706
10"	1197	0	10	-30	40	163759	-13.2	149.1	0.010	31.4	250.8	1544
10"	1072	0	10	-30	45	144902	-13.2	149.1	0.011	31.4	250.8	1649
10"	950	0	10	-30	50	129570	-13.2	149.1	0.010	31.4	250.8	1607
10"	4206	5	10	-40	10	513027	-13.2	149.1	0.009	31.4	250.8	1388
10"	2865	5	10	-40	15	369297	-15.7	151.9	0.011	31.5	255.1	1679
10"	2118	5	10	-40	20	288123	-17.0	150.5	0.011	29.7	255.0	1697
10"	1695	5	10	-40	25	234760	-14.5	150.5	0.011	31.5	253.0	1714
10"	1395	5	10	-40	30	197520	-10.8	146.3	0.011	31.0	246.5	1783
10"	1186	5	10	-40	35	169888	-10.8	146.3	0.012	31.0	246.5	1874
10"	1039	5	10	-40	40	148226	-10.8	146.3	0.011	31.0	246.5	1734
10"	907	5	10	-40	45	131223	-41.8	147.7	0.012	9.4	270.5	1879
10"	817	5	10	-40	50	117260	-52.8	174.6	0.012	8.5	291.9	1925
10"	4140	5	10	-30	10	513837	-13.2	149.1	0.008	31.4	250.8	1248
10"	2834	5	10	-30	15	369492	-13.2	149.1	0.010	31.4	250.8	1587
10"	2132	5	10	-30	20	288165	-17.0	150.5	0.010	29.7	255.0	1518
10"	1664	5	10	-30	25	234816	-17.0	150.5	0.011	29.7	255.0	1707
10"	1385	5	10	-30	30	197534	-13.2	149.1	0.012	31.4	250.8	1930
10"	1170	5	10	-30	35	169794	-10.8	146.3	0.011	31.0	246.5	1685
10"	1019	5	10	-30	40	148213	-10.8	146.3	0.011	31.0	246.5	1725
10"	896	5	10	-30	45	131071	-41.8	147.7	0.011	9.4	270.5	1664
10"	825	5	10	-30	50	117105	-52.8	174.6	0.010	8.5	291.9	1638
10"	3701	10	10	-40	10	460484	-13.2	149.1	0.009	31.4	250.8	1368
10"	2510	10	10	-40	15	331552	-13.2	149.1	0.011	31.4	250.8	1792
10"	1847	10	10	-40	20	258813	-13.2	149.1	0.012	31.4	250.8	1873
10"	1470	10	10	-40	25	210756	-13.2	149.1	0.011	31.4	250.8	1742
10"	1228	10	10	-40	30	177191	-13.2	149.1	0.012	31.4	250.8	1898
10"	1036	10	10	-40	35	152561	-10.8	146.3	0.012	31.0	246.5	1809
10"	897	10	10	-40	40	133018	-10.8	146.3	0.011	31.0	246.5	1784
10"	788	10	10	-40	45	117685	-13.2	149.1	0.012	31.4	250.8	1811
10"	710	10	10	-40	50	105184	-52.8	174.6	0.013	8.5	291.9	2025
10"	3662	10	10	-30	10	461202	-13.2	149.1	0.009	31.4	250.8	1484
10"	2499	10	10	-30	15	331651	-13.2	149.1	0.010	31.4	250.8	1629
10"	1846	10	10	-30	20	258767	-13.2	149.1	0.011	31.4	250.8	1740
10"	1456	10	10	-30	25	210719	-12.0	144.8	0.011	29.2	246.6	1679
10"	1209	10	10	-30	30	177340	-13.2	149.1	0.011	31.4	250.8	1749
10"	1016	10	10	-30	35	152334	-10.8	146.3	0.010	31.0	246.5	1597
10"	877	10	10	-30	40	133015	-10.8	146.3	0.011	31.0	246.5	1795
10"	776	10	10	-30	45	117626	-13.2	149.1	0.012	31.4	250.8	1906
10"	699	10	10	-30	50	105089	-52.8	174.6	0.012	8.5	291.9	1829
36"	5524	0	10	-40	10	565454	19.5	94.2	0.008	1.5	191.7	1198
36"	3883	0	10	-40	15	407089	-13.2	149.1	0.010	31.4	250.8	1607
36"	2952	0	10	-40	20	317640	-17.0	150.5	0.011	29.7	255.0	1688
36"	2339	0	10	-40	25	258942	-13.2	149.1	0.012	31.4	250.8	1803
36"	1986	0	10	-40	30	217864	-13.2	149.1	0.012	31.4	250.8	1877
36"	1705	0	10	-40	35	187407	-10.8	146.3	0.012	31.0	246.5	1805
36"	1504	0	10	-40	40	163557	-10.8	146.3	0.010	31.0	246.5	1622
36"	1354	0	10	-40	45	144706	-30.0	153.3	0.012	21.5	266.6	1850
36"	1211	0	10	-40	50	129443	-13.2	149.1	0.012	31.4	250.8	1835
36"	5538	0	10	-30	10	566450	-17.0	150.5	0.007	29.7	255.0	1064

(1)	(2)	(3)	(4)	(5)	(6)	(7)	(8)	(9)	(10)	(11)	(12)	(13)
\dots / \dots												
36"	3853	0	10	-30	15	407404	-13.2	149.1	0.010	31.4	250.8	1575
36"	2926	0	10	-30	20	317723	-17.0	147.7	0.011	27.8	252.8	1733
36"	2346	0	10	-30	25	259017	-17.0	150.5	0.011	29.7	255.0	1661
36"	1967	0	10	-30	30	217920	-13.2	149.1	0.012	31.4	250.8	1838
36"	1694	0	10	-30	35	187315	-10.8	146.3	0.010	31.0	246.5	1603
36"	1500	0	10	-30	40	163469	-10.8	146.3	0.011	31.0	246.5	1774
36"	1309	0	10	-30	45	144627	-10.8	146.3	0.011	31.0	246.5	1757
36"	1201	0	10	-30	50	129333	-52.8	174.6	0.010	8.5	291.9	1529
36"	4870	5	10	-40	10	512341	-13.2	149.1	0.008	31.4	250.8	1278
36"	3385	5	10	-40	15	368743	-17.0	150.5	0.011	29.7	255.0	1666
36"	2567	5	10	-40	20	287636	-17.0	150.5	0.011	29.7	255.0	1673
36"	2039	5	10	-40	25	234433	-17.0	150.5	0.011	29.7	255.0	1789
36"	1705	5	10	-40	30	197226	-13.2	149.1	0.012	31.4	250.8	1849
36"	1486	5	10	-40	35	169697	-10.8	146.3	0.012	31.0	246.5	1810
36"	1307	5	10	-40	40	147984	-10.8	146.3	0.011	31.0	246.5	1712
36"	1152	5	10	-40	45	130967	-41.8	147.7	0.012	9.4	270.5	1813
36"	1044	5	10	-40	50	117024	-52.8	174.6	0.012	8.5	291.9	1900
36"	4871	5	10	-30	10	513206	-17.0	150.5	0.008	29.7	255.0	1316
36"	3364	5	10	-30	15	368971	-17.0	150.5	0.010	29.7	255.0	1624
36"	2540	5	10	-30	20	287669	-17.0	150.5	0.011	29.7	255.0	1681
36"	2032	5	10	-30	25	234444	-17.0	150.5	0.010	29.7	255.0	1641
36"	1697	5	10	-30	30	197264	-13.2	149.1	0.012	31.4	250.8	1832
36"	1449	5	10	-30	35	169581	-10.8	146.3	0.011	31.0	246.5	1653
36"	1298	5	10	-30	40	147896	-10.8	146.3	0.011	31.0	246.5	1723
36"	1136	5	10	-30	45	130876	-32.8	153.3	0.011	19.2	268.4	1747
36"	1026	5	10	-30	50	116899	-52.8	174.6	0.011	8.5	291.9	1759
36"	4274	10	10	-40	10	459885	-13.2	149.1	0.009	31.4	250.8	1468
36"	2949	10	10	-40	15	331159	-14.5	150.5	0.012	31.5	253.0	1866
36"	2225	10	10	-40	20	258390	-13.2	149.1	0.012	31.4	250.8	1859
36"	1776	10	10	-40	25	210492	-13.2	149.1	0.012	31.4	250.8	1844
36"	1498	10	10	-40	30	176937	-13.2	149.1	0.013	31.4	250.8	1994
36"	1276	10	10	-40	35	152192	-10.8	146.3	0.012	31.0	246.5	1876
36"	1119	10	10	-40	40	132733	-10.8	146.3	0.011	31.0	246.5	1735
36"	986	10	10	-40	45	117577	-13.2	149.1	0.012	31.4	250.8	1898
36"	889	10	10	-40	50	104990	-52.8	174.6	0.013	8.5	291.9	2022
36"	4279	10	10	-30	10	460601	-13.2	149.1	0.009	31.4	250.8	1476
36"	2950	10	10	-30	15	331374	-13.2	149.1	0.012	31.4	250.8	1817
36"	2207	10	10	-30	20	258442	-13.2	149.1	0.012	31.4	250.8	1813
36"	1756	10	10	-30	25	210444	-13.2	149.1	0.011	31.4	250.8	1722
36"	1484	10	10	-30	30	177007	-13.2	149.1	0.012	31.4	250.8	1843
36"	1280	10	10	-30	35	152135	-13.2	149.1	0.011	31.4	250.8	1767
36"	1116	10	10	-30	40	132757	-13.2	149.1	0.011	31.4	250.8	1775
36"	981	10	10	-30	45	117455	-54.3	174.4	0.010	7.0	292.2	1615
36"	889	10	10	-30	50	104867	-52.8	174.6	0.012	8.5	291.9	1823

Table 10. 3D linear estimator, NVSUMSS cross-correlated with 2MRS to remove local sources (uses healpy grid of $nside = 32$) (1) Angular tolerance within which 2MRS sources are looked for, (2) Number of sources removed because of 2MRS overlap, (3) Supergalactic latitude cut(\pm), (4) Galactic Latitude Cut(\pm), (5) NVSS-SUMSS patch declination, (6) Flux threshold (mJy), (7) Total Number of sources left after cuts, (8) dipole DEC(deg), (9) dipole RA(deg), (10) dipole value, (11) Galactic b (deg), (12) Galactic l (deg), (13) Velocity (km s^{-1})

(1)	(2)	(3)	(4)	(5)	(6)	(7)	(8)	(9)	(10)	(11)	(12)	(13)
1"	1042	0	10	-40	10	569975	20.0	128.3	2726	31.0	204.8	1121
1"	835	0	10	-40	15	410131	6.4	139.1	2159	35.0	224.8	1234
1"	683	0	10	-40	20	319894	-0.1	140.9	1885	33.2	232.6	1381
1"	583	0	10	-40	25	260710	-2.1	145.8	1536	36.1	238.0	1381
1"	480	0	10	-40	30	219373	-3.8	149.5	1346	38.0	242.6	1438
1"	415	0	10	-40	35	188687	-10.8	146.7	1003	31.3	247.0	1246
1"	370	0	10	-40	40	164696	-13.9	143.4	985	26.8	247.1	1402
1"	322	0	10	-40	45	145733	-17.4	150.9	851	29.7	255.7	1369
1"	283	0	10	-40	50	130371	-19.3	165.2	786	36.4	269.9	1413
1"	987	0	10	-30	10	570995	3.6	122.1	2341	18.7	218.6	961
1"	793	0	10	-30	15	410465	-1.0	138.7	2019	30.9	232.2	1153
1"	645	0	10	-30	20	320006	-4.6	138.1	1670	28.4	235.2	1223
1"	544	0	10	-30	25	260819	-8.7	138.0	1368	25.9	239.0	1229
1"	460	0	10	-30	30	219429	-6.0	144.4	1276	32.6	240.8	1362
1"	396	0	10	-30	35	188605	-8.1	142.2	982	29.6	241.2	1221
1"	342	0	10	-30	40	164620	-13.3	136.8	884	22.3	242.2	1258
1"	311	0	10	-30	45	145654	-13.7	149.4	845	31.3	251.5	1360
1"	267	0	10	-30	50	130261	-16.0	161.9	704	37.4	264.4	1266
1"	933	5	10	-40	10	516312	15.9	128.6	2523	29.8	209.4	1145
1"	751	5	10	-40	15	371449	1.4	137.5	2045	31.1	229.0	1290
1"	606	5	10	-40	20	289591	-4.3	136.9	1681	27.6	234.2	1360
1"	513	5	10	-40	25	235989	-7.3	138.5	1388	27.2	238.0	1379
1"	430	5	10	-40	30	198406	-6.2	145.2	1138	33.1	241.6	1344
1"	373	5	10	-40	35	170731	-14.2	147.4	953	29.6	250.4	1308
1"	329	5	10	-40	40	148933	-17.2	142.2	876	23.8	249.1	1378
1"	283	5	10	-40	45	131819	-19.5	151.7	811	28.7	257.9	1442
1"	249	5	10	-40	50	117909	-28.3	155.9	762	24.2	267.5	1514
1"	888	5	10	-30	10	517106	2.6	121.2	2221	17.5	219.1	1006
1"	705	5	10	-30	15	371710	-4.0	134.1	1897	25.4	232.1	1196
1"	577	5	10	-30	20	289669	-7.7	132.9	1550	22.3	234.9	1254
1"	485	5	10	-30	25	236033	-8.1	134.6	1301	23.5	236.2	1292
1"	408	5	10	-30	30	198550	-12.1	138.7	1150	24.5	242.4	1357
1"	352	5	10	-30	35	170655	-10.7	146.2	871	31.0	246.4	1196
1"	306	5	10	-30	40	148891	-15.9	134.4	858	18.8	242.9	1350
1"	269	5	10	-30	45	131772	-20.1	144.7	734	23.6	253.2	1306
1"	233	5	10	-30	50	117720	-21.0	156.4	642	30.4	263.0	1279
1"	818	10	10	-40	10	463382	10.4	128.8	2460	27.8	215.2	1244
1"	654	10	10	-40	15	333458	0.5	133.4	1848	27.1	227.5	1299
1"	529	10	10	-40	20	260082	-7.9	128.8	1590	18.8	232.7	1432
1"	451	10	10	-40	25	211769	-5.3	132.4	1282	23.2	232.3	1419
1"	374	10	10	-40	30	178072	-5.5	133.8	1159	24.3	233.4	1526
1"	319	10	10	-40	35	153157	-11.2	134.3	956	21.5	238.9	1463
1"	285	10	10	-40	40	133641	-16.1	130.2	888	15.5	240.6	1558
1"	250	10	10	-40	45	118275	-14.4	141.8	813	25.4	246.4	1612
1"	220	10	10	-40	50	105680	-22.4	150.2	703	25.5	259.0	1559
1"	778	10	10	-30	10	464153	-3.5	124.7	2269	17.6	226.5	1146
1"	616	10	10	-30	15	333679	-6.8	131.8	1891	21.9	233.4	1328
1"	494	10	10	-30	20	260107	-8.7	125.6	1493	15.7	231.6	1345
1"	414	10	10	-30	25	211788	-6.0	132.4	1266	22.9	233.0	1401
1"	350	10	10	-30	30	178131	-8.1	132.3	1145	21.6	234.9	1507
1"	301	10	10	-30	35	153161	-13.7	127.6	874	14.7	237.2	1337
1"	262	10	10	-30	40	133563	-13.8	118.7	753	7.3	232.6	1321
1"	234	10	10	-30	45	118249	-15.5	134.7	774	19.3	242.7	1535
1"	204	10	10	-30	50	105618	-24.1	150.1	572	24.3	260.1	1270
1"	959	0	15	-40	10	511545	16.7	132.7	2370	33.7	210.3	1086
1"	771	0	15	-40	15	367925	3.7	143.8	2098	37.7	230.6	1337
1"	620	0	15	-40	20	286792	-2.8	145.6	1851	35.5	238.6	1513
1"	525	0	15	-40	25	233742	-6.3	150.9	1495	37.4	246.2	1499
1"	446	0	15	-40	30	196725	-7.0	148.9	1299	35.5	245.1	1548
1"	378	0	15	-40	35	169146	-12.1	150.7	1072	33.4	251.1	1485

(1)	(2)	(3)	(4)	(5)	(6)	(7)	(8)	(9)	(10)	(11)	(12)	(13)
\dots / \dots												
36"	4453	0	20	-30	10	451118	4.0	128.9	1592	25.0	221.7	827
36"	3108	0	20	-30	15	324342	-2.2	143.2	1636	34.0	236.4	1182
36"	2362	0	20	-30	20	252688	-5.5	140.6	1418	29.9	237.7	1315
36"	1890	0	20	-30	25	205974	-9.9	149.1	1174	33.7	248.0	1336
36"	1622	0	20	-30	30	173446	-8.8	147.8	1118	33.4	245.9	1510
36"	1396	0	20	-30	35	148977	-9.5	154.4	734	37.8	252.0	1155
36"	1227	0	20	-30	40	130089	-15.1	144.1	647	26.5	248.7	1165
36"	1087	0	20	-30	45	115063	-14.1	160.3	683	38.1	261.4	1392
36"	985	0	20	-30	50	102801	-12.4	168.6	610	44.0	269.0	1391
36"	3837	5	20	-40	10	403942	17.0	137.3	2005	37.9	211.9	1164
36"	2669	5	20	-40	15	290532	5.8	143.4	1703	38.4	228.1	1373
36"	2020	5	20	-40	20	226369	-3.0	141.9	1444	32.4	236.2	1495
36"	1624	5	20	-40	25	184527	-7.7	148.0	1182	34.3	245.1	1501
36"	1403	5	20	-40	30	155255	-7.7	149.8	992	35.7	246.5	1498
36"	1193	5	20	-40	35	133565	-17.5	155.2	801	32.4	259.3	1406
36"	1045	5	20	-40	40	116566	-18.3	147.2	704	26.5	253.5	1414
36"	923	5	20	-40	45	103135	-21.3	155.1	706	29.3	262.0	1605
36"	842	5	20	-40	50	92081	-24.3	169.7	638	33.9	277.3	1623
36"	3834	5	20	-30	10	404581	2.7	130.3	1662	25.5	223.7	963
36"	2663	5	20	-30	15	290794	-2.4	139.0	1571	30.4	233.8	1266
36"	2030	5	20	-30	20	226418	-7.7	135.3	1346	24.4	236.3	1393
36"	1618	5	20	-30	25	184525	-10.4	144.9	1007	30.3	245.2	1279
36"	1374	5	20	-30	30	155336	-12.3	146.6	886	30.2	248.1	1337
36"	1180	5	20	-30	35	133515	-16.6	151.0	805	30.3	255.1	1413
36"	1040	5	20	-30	40	116487	-15.0	143.6	617	26.3	248.2	1242
36"	917	5	20	-30	45	103014	-18.4	149.8	610	28.2	255.6	1388
36"	827	5	20	-30	50	91978	-20.2	171.5	573	38.3	277.1	1460
36"	3354	10	20	-40	10	358210	12.3	139.3	1905	37.9	218.4	1247
36"	2322	10	20	-40	15	257769	1.8	136.4	1564	30.4	227.9	1422
36"	1749	10	20	-40	20	200974	-7.9	133.0	1340	22.4	235.1	1563
36"	1405	10	20	-40	25	163641	-6.1	138.7	968	28.0	237.0	1387
36"	1193	10	20	-40	30	137671	-4.3	142.7	925	32.3	238.0	1574
36"	1012	10	20	-40	35	118483	-22.5	144.6	740	21.9	255.0	1463
36"	895	10	20	-40	40	103343	-17.5	138.9	632	21.2	247.1	1434
36"	785	10	20	-40	45	91428	-17.7	148.6	667	27.9	254.1	1710
36"	715	10	20	-40	50	81613	-24.7	160.4	600	29.5	268.8	1722
36"	3334	10	20	-30	10	358656	1.8	131.7	1738	26.3	225.3	1136
36"	2316	10	20	-30	15	257979	-5.2	137.5	1400	27.5	235.5	1272
36"	1761	10	20	-30	20	200972	-10.6	130.8	1261	19.0	236.2	1471
36"	1387	10	20	-30	25	163666	-8.9	136.2	978	24.3	237.9	1401
36"	1187	10	20	-30	30	137802	-9.8	136.5	942	24.1	239.0	1603
36"	1007	10	20	-30	35	118372	-17.2	136.3	681	19.5	245.2	1349
36"	878	10	20	-30	40	103290	-15.8	135.6	554	19.8	243.6	1257
36"	783	10	20	-30	45	91364	-14.6	145.4	639	27.9	249.1	1639
36"	703	10	20	-30	50	81496	-19.6	168.4	545	37.6	273.5	1567